Astronomy & Astrophysics

Anisotropy of plasma turbulence at ion scales: Hall and pressure–strain effects

Petr Hellinger[1,2], Andrea Verdini[3,4], Victor Montagud-Camps[5], Luca Franci[6], Emanuele Papini[7], Lorenzo Matteini[6], and Simone Landi[3,4]

[1] Astronomical Institute of the Czech Academy of Sciences, Prague, Czech Republic
  e-mail: petr.hellinger@asu.cas.cz
[2] Institute of Atmospheric Physics of the Czech Academy of Sciences, Prague, Czech Republic
[3] Dipartimento di Fisica e Astronomia, Florence University, Florence, Italy
[4] INAF – Osservatorio Astrofisico di Arcetri, Florence, Italy
[5] Department of Electromagnetism and Electronics, University of Murcia, Murcia, Spain
[6] Imperial College, London, UK
[7] INAF – Istituto di Astrofisica e Planetologia Spaziali, Roma, Italy

ABSTRACT

Aims. We investigated the properties of plasma turbulence at ion scales in the solar wind context. We concentrated on the behaviour of the Hall physics and the pressure strain interaction and their anisotropy owing to the ambient magnetic field.
Methods. We studied the results of a three-dimensional hybrid simulation of decaying plasma turbulence using the Kármán–Howarth–Monin (KHM) equation, which quantifies different turbulent processes.
Results. The isotropised KHM analysis shows that kinetic plus magnetic (kinetic+magnetic) energy decays at large scales; this energy cascades from large to small scales via the magneto-hydrodynamic non-linearity that is partly continued via the Hall coupling around the ion scales. The cascading kinetic+magnetic energy is partly dissipated at small scales via resistive dissipation. This standard dissipation is complemented by the pressure–strain interaction, which plays the role of an effective dissipation mechanism and starts to act at relatively large scales. The pressure–strain interaction has two components, compressive and incompressive. Compressive interaction is connected with the velocity dilatation, which mostly reversibly exchanges kinetic+magnetic and internal energies. Incompressive interaction mostly irreversibly converts the kinetic+magnetic energy to internal energy. The compressive effects lead to important oscillations of the turbulence properties, but the compressibility is strongly reduced when averaged over a time period spanning a few periods of the oscillations. The ambient magnetic field induces a strong spectral anisotropy. The turbulent fluctuations exhibit larger scales along the magnetic field compared to the perpendicular directions. The KHM results show the corresponding anisotropy of turbulent processes: their characteristic scales shift to larger scales in the quasi-parallel direction with respect to the ambient magnetic field compared to the quasi-perpendicular direction. This anisotropy is weak at large scales owing to the initial isotropic spectrum, and becomes progressively stronger at small scales.

Key words. solar wind

1. Introduction

Plasma turbulence in the presence of a sufficiently strong background magnetic field $\boldsymbol{B}_0$ exhibits a spectral anisotropy: fluctuating energy is concentrated in modes with strongly oblique wave-vectors with respect to $\boldsymbol{B}_0$ (Montgomery & Turner 1981; Shebalin et al. 1983; Ghosh & Goldstein 1997). This anisotropy is not well understood; we have phenomenological approaches such as those based on geometric decompositions, for example two-dimensional (2D) plus slab, or conjectures like critical balance (Matthaeus et al. 1990; Goldreich & Sridhar 1995; Oughton et al. 2015; Oughton & Matthaeus 2020). To avoid the need of such ad hoc assumptions we can characterise turbulence and its anisotropy using the Kármán–Howarth–Monin (KHM) equation starting from first principles. It was derived in the incompressible, constant density approximation, first for hydrodynamic turbulence (de Kármán & Howarth 1938; Monin & Yaglom 1975), and then extended to magneto-hydrodynamic (MHD) turbulence (Politano & Pouquet 1998a,b) and Hall MHD (Galtier 2008;

Hellinger et al. 2018; Ferrand et al. 2019). This equation quantifies different processes. In a decaying (non-driven) system, this equation gives the rate of losses (decay) of energy at large scales (in the energy-containing range), the cross-scale energy transfer (cascade), as well as the dissipation. This equation is formulated in the separation space of increments, which gives a natural possibility for investigation of turbulence anisotropy in the separation space looking at increments parallel and perpendicular to the background magnetic field $\boldsymbol{B}_0$.

Results of the KHM analysis of direct simulation of MHD turbulence (Verdini et al. 2015) show a clear anisotropy of structure functions in the separation space $(l_\perp, l_\parallel)$. This work also highlights the somewhat paradoxical properties of turbulence in magnetised plasmas. The inertial range can be formally defined as the region where the cascade rate K is equal to the dissipation rate Q. The simulation results of Verdini et al. (2015) clearly exhibit a tendency to have $K(l_\perp, l_\parallel) = Q$ within a range of scales that is anisotropically distributed in the $(l_\perp, l_\parallel)$ space. In the isotropic case K just expresses the cascade rate, while in the anisotropic case this quantity characterises the cascade rate

but does not have any information about the direction of energy cascade in the ($l_\perp$, $l_\parallel$) space.

To describe the cross-scale energy transfer in turbulence spectral or spatial filtering (Eyink & Aluie 2009; Aluie 2011; Grete et al. 2017) techniques are also used. In this case, however, filters are usually assumed to be isotropic; when anisotropic spatial filtering (coarse graining) is used the cascade rate exhibits an anisotropy (Manzini et al. 2022) that is similar to the KHM results.

For weakly collisional plasmas (such as those in the solar wind), it is necessary to include the effects of plasma compressibility (Hellinger et al. 2021a) and treat the pressure as a tensor (Hellinger et al. 2022). The pressure–strain interaction, which couples the magnetic+kinetic energy to the internal energy (Del Sarto et al. 2016), may work as an effective dissipation channel, as seen in direct kinetic numerical simulations (Yang et al. 2017; Matthaeus et al. 2020; Hellinger et al. 2022; Arró et al. 2022).

Numerical simulations and in situ observations suggest that the pressure–strain channel is likely responsible for correlations between particle velocity-field gradients and temperatures (Franci et al. 2016; Parashar & Matthaeus 2016; Pezzi et al. 2021; Yordanova et al. 2021), but its properties are not well understood. Many different physical processes contribute to this interaction (Yang et al. 2017; Cassak & Barbhuiya 2022), including those connected with plasma compression and expansion. It is not clear at what spatial scales the pressure–strain effect acts. Electron and ion energisations are expected to work at very different scales (Franci et al. 2022), but comparable scales are observed in some full-particle simulations (Yang et al. 2022). It is also unclear what the role of the turbulence anisotropy is (most of the present simulations are two-dimensional) and how it compares to other processes such as Hall coupling (Papini et al. 2019, 2021). In this paper we extended the two-dimensional work of Hellinger et al. (2022), we analysed a three-dimensional hybrid simulation of decaying plasma turbulence using the KHM equation, and we studied the anisotropy of different turbulent processes.

2. The Kármán–Howarth–Monin equation

2.1. Extended Hall magnetohydrodynamics

We investigated a system governed by the following extended compressible inviscid Hall MHD equations for the plasma density ρ, the plasma mean velocity $\boldsymbol{u}$, and the magnetic field $\boldsymbol{B}$:

$$\partial_t \rho + (\boldsymbol{u} \cdot \boldsymbol{\nabla})\rho = -\rho \boldsymbol{\nabla} \cdot \boldsymbol{u},$$
$$\rho \partial_t \boldsymbol{u} + \rho(\boldsymbol{u} \cdot \boldsymbol{\nabla})\boldsymbol{u} = \boldsymbol{J} \times \boldsymbol{B} - \boldsymbol{\nabla} \cdot \mathbf{P}, \qquad (1)$$
$$\partial_t \boldsymbol{B} = \boldsymbol{\nabla} \times [(\boldsymbol{u} - \boldsymbol{j}) \times \boldsymbol{B}] + \eta \nabla^2 \boldsymbol{B}.$$

Here $\mathbf{P}$ is the plasma pressure tensor, η is the electric resistivity, $\boldsymbol{J}$ is the electric current density, $\boldsymbol{j}$ is the electric current density in velocity units, and $\boldsymbol{j} = \boldsymbol{J}/\rho_c = \boldsymbol{u} - \boldsymbol{u}_e$ (ρ_c and $\boldsymbol{u}_e$ being the ion charge density and the electron velocity, respectively). We assume SI units except for the magnetic permeability μ_0, which is set to one (SI results can be obtained by the rescaling $\boldsymbol{B} \rightarrow \boldsymbol{B}\mu_0^{-1/2}$). Equation (1) (except the resistive term) can be derived taking moments of the Vlasov equation for protons and electrons, and assuming massless electrons. We added a resistive dissipation, as used in the hybrid code to avoid the accumulation of energy on small scales; this process substitutes the electron dissipation. The plasma pressure tensor contains contributions from protons and electrons but for electrons we further adopted a scalar pressure (an approximation used in the hybrid code).

For the sum of kinetic ($E_{kin} = \langle \rho |\boldsymbol{u}|^2/2 \rangle$) and magnetic ($E_{mag} = \langle |\boldsymbol{B}|^2/2 \rangle$) energies (averaged over a closed volume) we obtained this budget equation,

$$\partial_t \left(E_{kin} + E_{mag}\right) = \langle \mathbf{P} : \boldsymbol{\nabla}\boldsymbol{u} \rangle - \eta \langle |\boldsymbol{J}|^2 \rangle, \qquad (2)$$

where the colon (:) operator denotes a double contraction of two tensors (i.e., for two tensors $\mathbf{T}$ and $\mathbf{V}$, $\mathbf{T} : \mathbf{V} = \sum_{ij} T_{ij} V_{ij}$, T_{ij} and V_{ij} being their components) and the angle brackets $\langle \bullet \rangle$ denote the averaging. The kinetic and magnetic energy is transferred to the internal energy by the resistive dissipation rate

$$Q_\eta = \eta \langle |\boldsymbol{J}|^2 \rangle. \qquad (3)$$

The exchanges between the kinetic+magnetic energy and the internal energy also proceed through the pressure–strain coupling. We defined the pressure–strain rate as

$$\psi = -\langle \mathbf{P} : \boldsymbol{\nabla}\boldsymbol{u} \rangle. \qquad (4)$$

Since the pressure–strain may behave as an effective dissipation rate, we defined the total (effective) dissipation rate as a sum of the two:

$$Q = Q_\eta + \psi. \qquad (5)$$

We did not consider an explicit viscosity since it is not present in the hybrid approximation.

2.2. The KHM equation

For the formulation of the KHM equation in terms of structure functions for compressible Hall MHD, we used the density-weighted velocity field $\boldsymbol{w} = \rho^{1/2}\boldsymbol{u}$ (Kida & Orszag 1990) to take into account a variable density. We characterised the spatial scale decomposition of the kinetic and magnetic energies (and their sum) using the second-order structure functions

$$S_w = \frac{1}{4} \left\langle |\delta\boldsymbol{w}|^2 \right\rangle, \quad S_B = \frac{1}{4} \left\langle |\delta\boldsymbol{B}|^2 \right\rangle, \quad \text{and} \quad S = S_w + S_B,$$

where the deltas denote increments of the corresponding quantities (e.g., $\delta\boldsymbol{w} = \boldsymbol{w}(\boldsymbol{x} + \boldsymbol{l}) - \boldsymbol{w}(\boldsymbol{x})$, $\boldsymbol{x}$ being the position and $\boldsymbol{l}$ the separation vector).

For the second-order structure function S representing the sum of the kinetic and magnetic energies, we derived the KHM equation in the form

$$\partial_t S = K_{MHD} + K_{Hall} - \Psi - D, \qquad (6)$$

where K_{MHD} and K_{Hall} are the MHD and Hall cascade rates, respectively; Ψ represents the pressure–strain effect; and D accounts for the effects of dissipation and heating. The cascade rates K_{MHD} and K_{Hall} (as well as Ψ and D) can be expressed in a few different equivalent forms. Here we used a form that uses increments of second-order quantities (equivalent to the usual form involving divergence of a third-order structure function vector; cf. Hellinger et al. 2021a):

$$K_{MHD} = -\frac{1}{2}\left\langle \delta\boldsymbol{w} \cdot \delta\left[(\boldsymbol{u} \cdot \boldsymbol{\nabla})\boldsymbol{w} + \frac{1}{2}\boldsymbol{w}(\boldsymbol{\nabla} \cdot \boldsymbol{u})\right]\right\rangle$$
$$-\frac{1}{2}\left\langle \delta\boldsymbol{w} \cdot \delta\left(\frac{\boldsymbol{J} \times \boldsymbol{B}}{\sqrt{\rho}}\right)\right\rangle + \frac{1}{2}\left\langle \delta\boldsymbol{J} \cdot \delta(\boldsymbol{u} \times \boldsymbol{B})\right\rangle, \qquad (7)$$

$$K_{Hall} = -\frac{1}{2}\left\langle \delta\boldsymbol{J} \cdot \delta(\boldsymbol{j} \times \boldsymbol{B})\right\rangle, \qquad (8)$$

$$\Psi = -\frac{1}{2}\left\langle \delta\boldsymbol{w} \cdot \delta\left(\frac{\boldsymbol{\nabla} \cdot \mathbf{P}}{\sqrt{\rho}}\right)\right\rangle, \qquad (9)$$

$$D = \frac{1}{2}\eta\left\langle |\delta\boldsymbol{J}|^2 \right\rangle = Q_\eta - \frac{1}{2}\eta\nabla^2 S_B. \qquad (10)$$

3. Simulation results

Here we analysed results of three-dimensional (3D) hybrid simulations of decaying plasma turbulence. In the hybrid approximation, ions are described by a particle-in-cell model, whereas electrons are a massless charge neutralising fluid (Matthews 1994; Franci et al. 2018a,b)[1] The system is numerically integrated in a 3D domain (x, y, z) with 512^3 grid points and the spatial resolution $\Delta x = \Delta y = \Delta z = d_i/8$. Here d_i denotes the ion inertial length. Protons are initially isotropic with $\beta_i = 0.5$, β_i being the ion beta (i.e., the ratio of the ion to magnetic pressures). In order to reduce the noise, a Gaussian smoothing on 3×3 points is used on the proton density and velocity in the code. A uniform ambient magnetic field $\boldsymbol{B}_0$, directed along z is present, whereas neutralising electrons are assumed to be isothermal with $\beta_e = \beta_i$; here β_e denotes the electron beta, the ratio of the electron and magnetic pressures. The system was initialised with an isotropic 3D spectrum of modes with random phases, linear Alfvén polarisation ($\delta \boldsymbol{B} \perp \boldsymbol{B}_0$), and vanishing correlation between magnetic field and velocity fluctuations. These modes were in the range $k \leq 0.22 d_i^{-1}$ with rms fluctuations $\delta B = 0.25$. The time step is $\Delta t = 0.005\Omega_i^{-1}$ for particle integration (the magnetic field is advanced with a smaller time step $\Delta t_B = \Delta t/20$), the number of particles per cell $N_{ppc} = 4096$, and a small resistivity $\eta = 10^{-3}\mu_0 v_A^2/\Omega_i$ is used to avoid energy accumulation at the smallest scales; we note that no explicit viscosity is present in the hybrid model. Here Ω_i denotes the ion cyclotron frequency, μ_0 is the magnetic permeability of the vacuum, and v_A stands for the Alfvén velocity. We let the system evolve until turbulence becomes quasi-stationary.

In the simulation, the proton kinetic energy E_{kin} and the magnetic energy E_{mag} oscillate with opposite phases, thus suggesting energy exchanges. However, overall these two quantities decrease. On the other hand, the proton internal energy, $E_{int} = 3\langle p \rangle/2$ increases (here p is the scalar pressure, $p = \mathrm{tr}(\mathbf{P})$, tr being the trace). This energisation works throughout the simulation even before turbulence is well developed. The total energy $E_{tot} = E_{kin} + E_{int} + E_{mag}$ slowly decreases owing to the resistive dissipation since electrons are assumed to be massless and isothermal. This behaviour is shown on Fig. 1a, which displays the evolution of relative changes of the kinetic, magnetic, and internal energies $\Delta E_{kin,mag,int,tot}$ given by $\Delta E(t) = [E(t) - E(0)]/E_{tot}(0)$. The proton energisation is driven by the pressure–strain coupling that plays the role of an effective dissipation channel. Figure 1b shows the resistive dissipation rate Q_η as a function of time as well as the two contributions to the pressure–strain rate ψ, the compressive contribution (Yang et al. 2017)

$$\psi_c = -\langle p \boldsymbol{\nabla} \cdot \boldsymbol{u} \rangle, \tag{11}$$

and the incompressive contribution $\psi_i = \psi - \psi_c$. These terms are normalised to the total effective dissipation rate $Q = 7.15 \times 10^{-5} m_p v_A^2 \Omega_i$ obtained by averaging $\psi + Q_\eta$ over the time interval $200 \leq t\Omega_i \leq 300$. The resistive dissipation rate Q_η starts at zero, slowly increases, and becomes quasi-stationary for $t\Omega_i \gtrsim 200$. The effective dissipation rate ψ_i is initially dominant, and strongly and rapidly oscillates in time for $t\Omega_i \lesssim 50$; later on its oscillations become weaker and slower. At later times Q_η and ψ_i become comparable to ψ; during the interval $200 \leq t\Omega_i \leq 300$ the averaged $\psi_i \simeq 0.47Q$, whereas $Q_\eta \simeq 0.44Q$. The compressive component of the pressure–strain interaction ψ_c starts at zero (owing to the incompressive initialisation) and reaches values comparable to Q. At later times it oscillates around zero, so

---
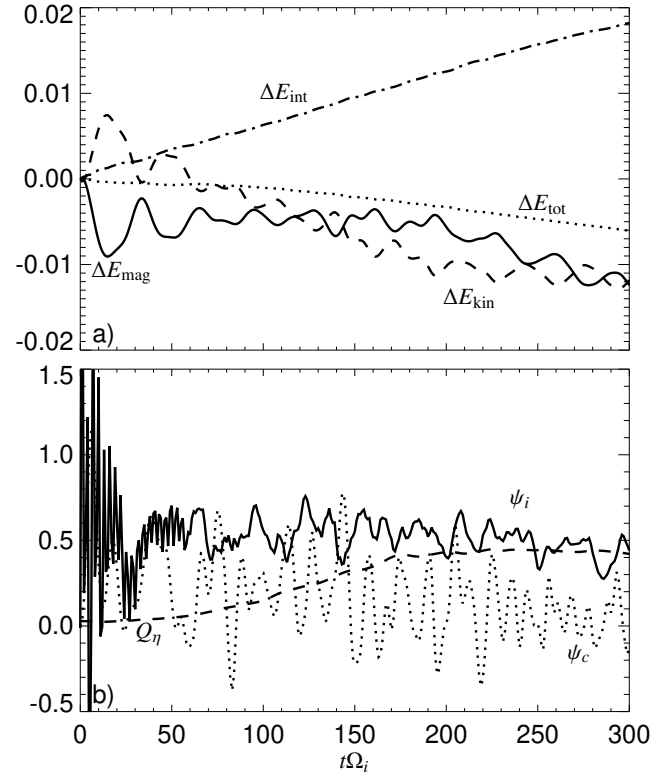
[1] See also http://www.asu.cas.cz/~helinger/camelia.html

Fig. 1. Evolution of different quantities as a function of time: (a) Relative changes in the kinetic energy ΔE_{kin} (dashed line), magnetic energy ΔE_{mag} (solid line), internal energy ΔE_{int} (dash-dotted line), and total energy ΔE_{tot} (dotted line); (b) resistive dissipation rate Q_η (dashed line), incompressive pressure–strain effective dissipation rate ψ_i (solid line), and its compressive counterpart ψ_c (dotted line). These rates are normalised to the total effective dissipation rate $Q = Q_\eta + \psi$ (averaged over $200 \leq t\Omega_i \leq 300$).

that its averaged value during the time interval $200 \leq t\Omega_i \leq 300$ is $\psi_c \simeq 0.08Q$.

The non-linear coupling between the magnetic and plasma velocity fields leads to a turbulent cascade. The value of Q_η becomes quasi-stationary for $t \gtrsim 170\Omega_i$ and we assume that the system reaches well-developed turbulence (Mininni & Pouquet 2009; Servidio et al. 2015).

4. Isotropic view

The turbulent cascade leads to a spread of fluctuating magnetic and kinetic energies over a wide range of scales. During the last quasi-stationary phase their spectral properties are only weakly varying. An example is given in Fig. 2 that shows omnidirectional power spectral densities of the magnetic field $\boldsymbol{B}$, P_B (in red), and the proton velocity field $\boldsymbol{w} = \rho^{1/2}\boldsymbol{u}$, P_w (in blue), and their sum P (in black) as a function of k. The magnetic spectrum is roughly Kolmogorov-like ($\propto k^{-5/3}$) at large scales with a break at around $kd_i \sim 3$ where it steepens. The proton kinetic spectrum has a somewhat steeper slope at large scales compared to P_B with a break at around $kd_i \sim 1$ where it strongly steepens. For $kd_i \gtrsim 5$ the kinetic spectrum is affected by the numerical noise connected with the finite number of particles per cell. The magnetic spectrum is also influenced by the noise and this effect is important for $kd_i \gtrsim 10$.

We can test turbulence properties in more detail using the KHM equation. While the background magnetic field leads to an important spectral anisotropy (as we discuss later), for the
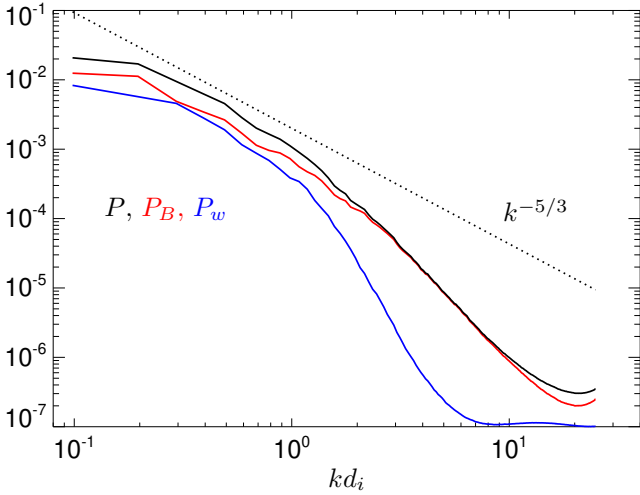
Fig. 2. Omnidirectional power spectral densities of the magnetic field $\boldsymbol{B}$, P_B (red), and the compensated proton velocity field $\boldsymbol{w}$, P_w (blue), and their sum P (black) as a function of k normalised to d_{i} at $t = 250\Omega_{\mathrm{i}}^{-1}$. The dotted line shows a spectrum $\propto k^{-5/3}$ for comparison.

Fig. 3. Schematic view of the theoretical expectations of a simplified system $0 = -\partial_t S + K - D$. The decay term $-\partial_t S$ (blue), the cascade rate K (green), and the dissipation rate $-D$ (red) are given as a function of l and are normalised to the dissipation rate Q.

assessment of the overall turbulence behaviour we start with isotropised quantities. Before we present the analysis of the simulation results via the KHM equation, we start with a presentation of the theoretical expectations. We assume a simplified model described with

$$\partial_t S = K - D, \tag{12}$$

where $\partial_t S$ represents the decay of the energy, K is the cascade rate, and D stands for the dissipation. The KHM equation has cumulative properties (Hellinger et al. 2021a,b, see also Appendix A), the two terms, $\partial_t S(l)$ and $D(l)$, behave as a spatial low-pass filter and correspond to the decay and dissipation rates on scales smaller than l. In contrast, the term K describes the cross-scale energy transfer (cascade) rate. Figure 3 shows the expected behaviour of the KHM terms as a function of l. The value of D starts at zero and increases towards Q. Above the dissipation length l_{diss}, where dissipation is not active, D is then constant: $D = Q$. In the ideal decaying case the system is stationary in the dissipation range and in the inertial range, and $\partial_t S$ is zero there. Only on large scales $l > l_{\mathrm{outer}}$ does this term become negative, $\partial_t S \rightarrow -Q$ (this is the energy containing range). Finally, between the dissipation length l_{diss} and the outer scale l_{outer} the cascade rate is constant, equal to the dissipation rate $K = Q$ (this relation is the formal definition of the inertial range).

The KHM equation constitutes a cross-scale energy conservation equation, and its application represents a strong validity check: one cannot expect that the KHM equation holds exactly in a numerical code. We defined the validity test O,

$$O = -\partial_t S + K_{\mathrm{MHD}} + K_{\mathrm{Hall}} - \Psi - D, \tag{13}$$

which measures the error of the code owing to numerical and other issues. Figure 4 displays the validity test and the different contributing terms ($-\partial_t S$, K_{MHD}, K_{Hall}, $-\Psi$, $-D$) normalised to the total effective dissipation rate Q as a function of the scale separation $l = |\boldsymbol{l}|$ (averaged over the quasi-stationary time period $200 \leq t\Omega_{\mathrm{i}} \leq 300$). Figure 4a shows that the KHM Eq. (6) is relatively well satisfied. The simulated system exhibits the expected behaviour, but is far from the ideal schema of Fig. 3. In this case there is no clear separation between the dissipation and
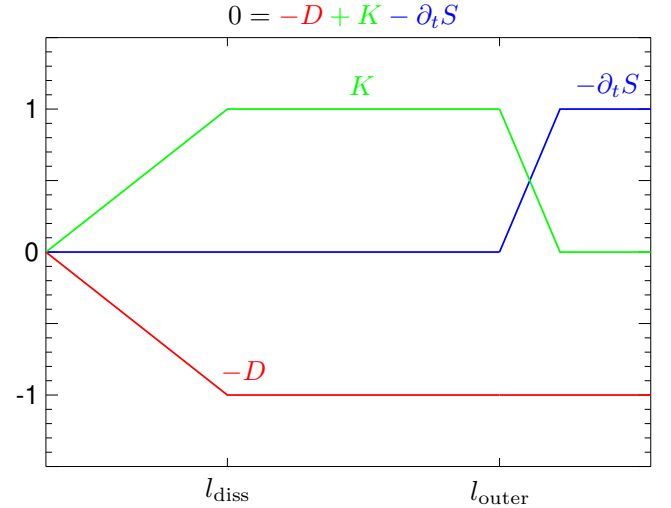
the energy containing ranges. The energy decay $\partial_t S$ is negative and important over a wide range of scales; it becomes negligible somewhat below $l = d_{\mathrm{i}}$. At the same time, the dissipation processes are active to larger scales. Consequently, the total cascade $K_{\mathrm{MHD}} + K_{\mathrm{Hall}}$ rate only reaches a maximum value of about one-half the dissipation rate Q. Figure 4b shows that the resistive dissipation is active on small scales $l \lesssim 2d_{\mathrm{i}}$, but that the pressure–strain interaction is active at relatively large scales, $l \lesssim 20d_{\mathrm{i}}$, largely extending the dissipation range. On intermediate scales the dominant process is the MHD cascade; K_{MHD} is negative at large scales, which indicates an inverse cascade. On small scales part of the cascade continues via the Hall term, K_{Hall} attains a maximum value of about 15% of Q.

Compressive effects contribute to the pressure–strain coupling and can be described as

$$\Psi_{\mathrm{c}} = -\frac{1}{2}\left\langle \delta\boldsymbol{w} \cdot \delta\left(\frac{\boldsymbol{\nabla}p}{\sqrt{\rho}}\right)\right\rangle \tag{14}$$

(see Eq. (9)). The magenta dashed line in Fig. 4 shows the Ψ_{c} contribution to Ψ as in the case of the pressure-dilatation term ψ_{c}, Ψ_{c} is weak when averaged over $200 \leq t\Omega_{\mathrm{i}} \leq 300$.

The KHM equation is valid during the whole simulation (it is relatively well satisfied $|O|/Q \lesssim 10\%$), so we can investigate how turbulence begins, evolves, and varies. Figure 5 shows the evolution of the isotropised KHM results, the different contributing terms as a function of time, and the separation scale $l = |\boldsymbol{l}|$ normalised to the total effective dissipation rate Q (averaged over the last third of the simulation $200 \leq t\Omega_{\mathrm{i}} \leq 300$).

Figure 5 demonstrates that the features of well-developed turbulence seen in Fig. 4 only appear at later times. During the turbulence onset (for about $t\Omega_{\mathrm{i}} \lesssim 200$) $\partial_t S$ is positive on intermediate scales. This means that the kinetic+magnetic energy increases in time on these scales owing to the MHD non-linear term (since $\partial_t S \sim K_{\mathrm{MHD}}$). At later times, $\partial_t S$ becomes negative, monotonically decreasing with l as expected for the cumulative low-pass filter property. The range where $\partial_t S$ is positive shifts with time to smaller scales as these are produced. As the energy transfer towards smaller scales continues, the resistive dissipation gradually appears. At later times we recover the cumulative properties of the resistive term D, increasing from 0 to about
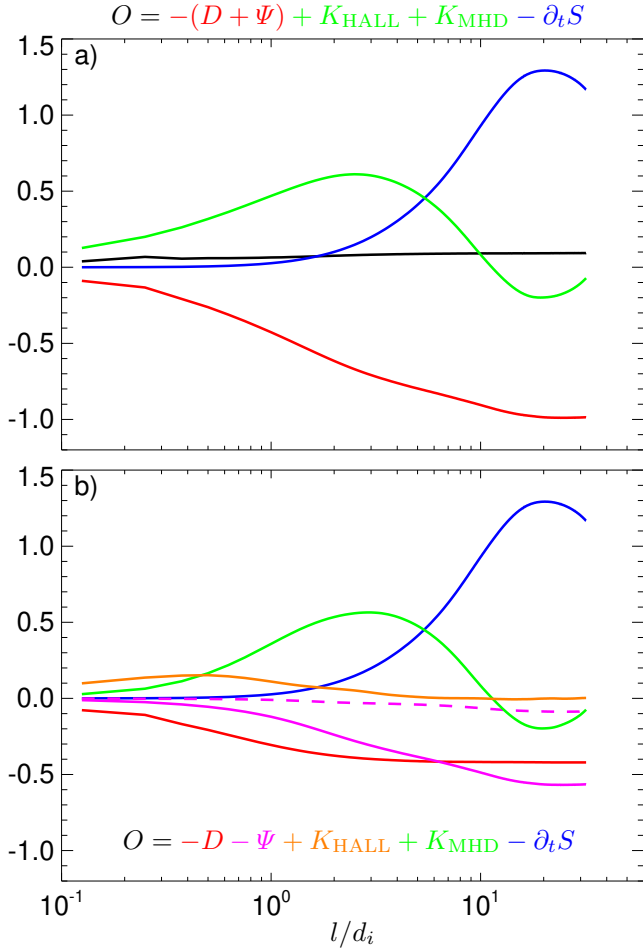
Fig. 4. Isotropised KHM analysis averaged results over a period of pressure–strain oscillations ($200 \le t\Omega_i \le 300$): (a) Validity test O (black line) as a function of l along with combined dissipative terms $-(D + \Psi)$ (red), combined cascade rates $K_{MHD} + K_{Hall}$ (green), and the decay rate $-\partial_t S$ (blue) in a format similar to Fig. 3. (b) Different separate contributing terms to the KHM equation: the decay rate $-\partial_t S$ (blue), the MHD cascade rate K_{MHD} (green), the Hall cascade rate K_{Hall} (orange), the resistive dissipation rate $-D$ (red), and the pressure–strain (effective dissipation) rate $-\Psi$ (magenta). The dashed magenta curve displays the compressive component of $-\Psi$. All the quantities are normalised to the time-averaged effective total dissipation rate Q.
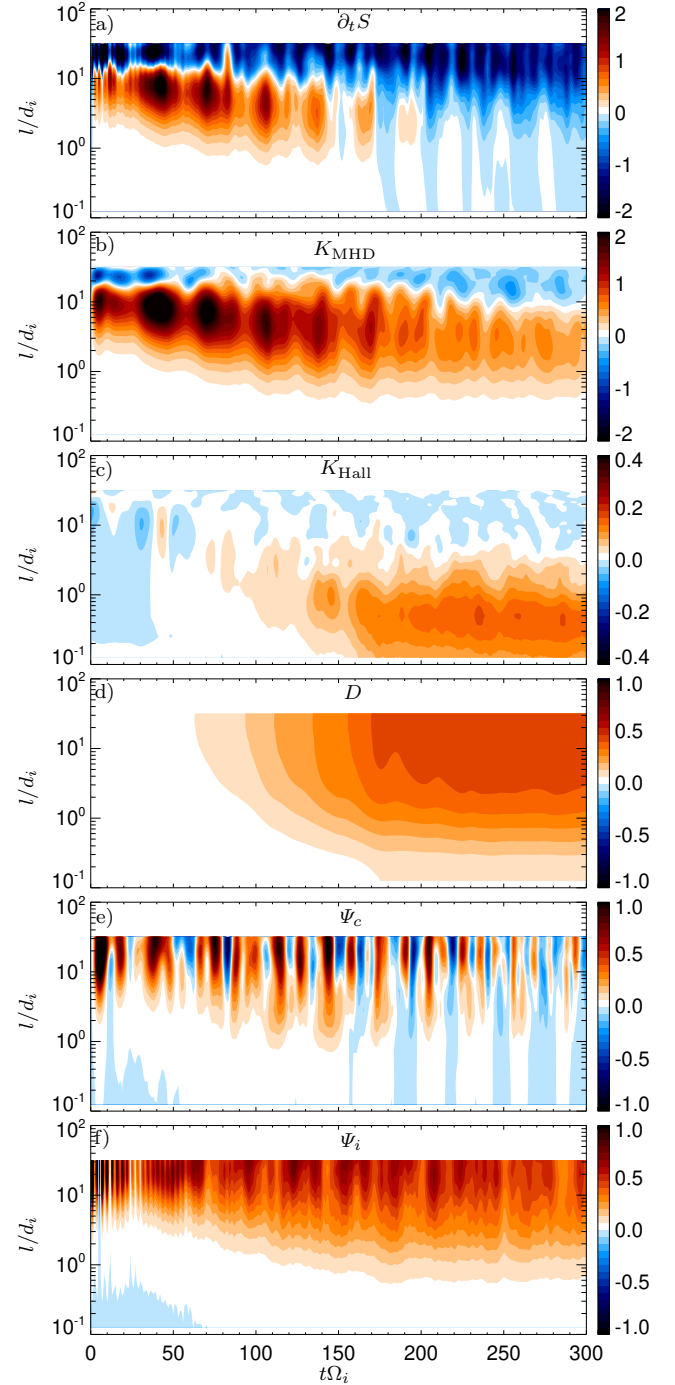

Fig. 5. Evolution of isotropised KHM results. Shown are the different KHM terms as a function of time t and l: (a) decay rate $\partial_t S$, (b) MHD cascade rate K_{MHD}, (c) Hall cascade rate K_{Hall}, (d) resistive dissipation rate D, (e) compressive pressure–strain rate Ψ_c, and (f) incompressive pressure–strain rate Ψ_i. All the quantities are normalised to the effective total dissipation rate Q.

a constant value for $l \gtrsim 2d_i$. The cross-scale energy transfer (cascade) rate K_{MHD} remains negative on large scales (which is a possible signature of an inverse cascade), but it is positive on intermediate scales indicating an energy transfer (cascade) from large to small scales. The range of positive K_{MHD} slowly shifts to smaller scales over time as these are produced. For $100 \lesssim t\Omega_i \lesssim 200$ positive values of K_{Hall} gradually appear as the Hall physics sets in.

The evolution of the pressure–strain interaction is more complicated. As in the case of pressure–strain rate, We split Ψ into its compressive part Ψ_c and the remaining $\Psi_i = \Psi - \Psi_c$, incompressive part (corresponding to the Pi-D term of Yang et al. 2017). The compressive contribution Ψ_c exhibits oscillations between about $-0.5Q$ and $0.5Q$ within a range of scales that extends to smaller scales as the cascade develops. Oscillations between positive and negative values indicate reversible exchanges between the magnetic+kinetic energy and the internal energy; as can be seen in Fig. 4, the average value of Ψ_c during $t\Omega_i \gtrsim 200$ is much weaker than its amplitude

of oscillation. In contrast, the incompressive part Ψ_i remains mostly positive; however, small negative values of both Ψ_i and Ψ_c for $t\Omega_i \lesssim 50$ suggest some weak opposite transfer on small scales. After a transient period (for $t\Omega_i \gtrsim 30$), Ψ_i monotonically increases with l (as expected for the cumulative low-pass filter) similarly to D; it works as an effective dissipation mechanism. The range where Ψ_i is active (i.e., where it strongly increases with l) shifts with time from large to intermediate scales. The
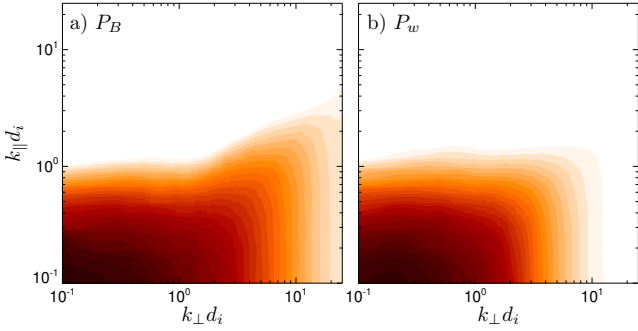
Fig. 6. Color scale plots of gyrotropised power spectral densities of (a) the magnetic energy P_B, and (b) the kinetic energy P_w as a function of $k_\perp$ and $k_\parallel$ (normalised to d_i).

system is quasi-stationary for $t\Omega_i \gtrsim 200$; the properties seen in Fig. 4 do not qualitatively change, but only exhibit some oscillations due to the compressive pressure–strain component Ψ_c.

We started with the spectral anisotropy of turbulent fluctuations. Figure 6 displays the (gyrotropised) power spectral densities of the magnetic energy P_B and the kinetic energy P_w as a function of $k_\perp$ and $k_\parallel$. Figure 6 shows that the power spectra are strongly anisotropic in the $(k_\perp, k_\parallel)$ plane, indicating a preferential cascade direction that is strongly oblique with respect to the ambient magnetic field $\boldsymbol{B}_0$. Similarly to the isotropised spectra, P_w decreases with $k_\perp$ faster than P_B. Their spectral anisotropies are weak on large scales (due to the initial isotropic spectrum) and increase towards small scales. The magnetic power spectrum P_B exhibits a change in behaviour for $k_\perp d_i \gtrsim 1$, a possible indication of the effect of the Hall term.

To analysed the different turbulent processes we used the full KHM equation where we gyrotropised the terms to obtain two-dimensional results as a function of $l_\parallel = |\boldsymbol{l} \cdot \boldsymbol{b}_0|$ and $l_\perp = |\boldsymbol{l} - (\boldsymbol{l} \cdot \boldsymbol{b}_0)\boldsymbol{b}_0|$ (where $\boldsymbol{b}_0 = \boldsymbol{B}_0/|\boldsymbol{B}_0|$). Figure 7 displays the anisotropic properties of the KHM equation, iso-contours of different quantities as a function of the separation scales $l_\perp$ and $l_\parallel$ (averaged over the time period $200 \leq t\Omega_i \leq 300$). Figure 7a shows the second-order structure function S as a reference (along with a circle $l_\perp^2 + l_\parallel^2 = $ const. to emphasise the anisotropy and the effect of the log-log plot); S decreases from large to small scales and exhibits a clear anisotropy with respect to the ambient magnetic field; at large scales S is weakly anisotropic (due to the isotropic initialisation) and the anisotropy increases towards smaller scales in agreement with the spectral properties of fluctuating magnetic and kinetic energies (see Fig. 6). The different terms in the KHM equation exhibit different anisotropic properties in the $(l_\perp, l_\parallel)$ plane, but their overall behaviours are similar to that of S: their anisotropy is weak on large scales and strong on small scales. Figure 7b shows the decaying term $\partial_t S$ that is important on large scales; its main anisotropy is that $|\partial_t S|$ decreases faster with decreasing $l_\parallel$. Figure 7c displays the MHD cascade rate K_{MHD}; the region where K_{MHD} dominates shifts to larger scales and shrinks when moving from the quasi-perpendicular to quasi-parallel angles. The sign of K_{MHD} becomes negative at large scales, which indicates some (anisotropic) inverse cascade. Figure 7d shows the Hall cascade rate K_{Hall}; the Hall cascade rate exhibits a strong anisotropy, the Hall cascade (and the Hall term) becomes important at larger scales for quasi-parallel angles compared to quasi-perpendicular ones. The shrinking and shifting of the MHD cascade rate K_{MHD} becomes less pronounced (but does not disappear) when we consider the total cascade rate $K = K_{MHD} + K_{Hall}$. Figure 7e displays the pressure–
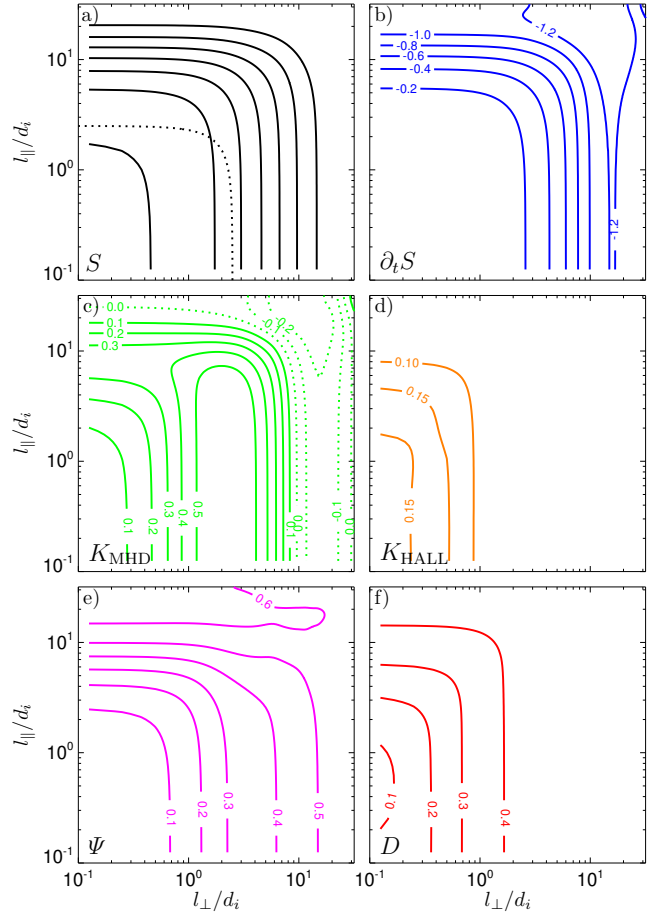
Fig. 7. Anisotropic KHM results, labelled iso-contours of different quantities as a function of the separation scales $l_\perp$ and $l_\parallel$ (averaged over the time period $200 \leq t\Omega_i \leq 300$): (a) Second-order structure function S, (b) Decay rate $\partial_t S$, (c) MHD cascade rate K_{MHD}, (d) Hall cascade rate K_{Hall}, (e) pressure–strain (effective dissipation) term Ψ, and (f) resistive dissipation term D. The dotted line in panel a displays a circle $l_\perp^2 + l_\parallel^2 = $ const. as a measure of anisotropy. The dotted lines in panel c denote non-positive values. The KHM quantities are normalised to the (time-averaged) effective total dissipation rate Q.

strain term Ψ. It exhibits a similar anisotropy to the Hall cascade rate on small scales but becomes more isotropic on intermediate scales; the range of scales where Ψ varies is narrower at quasi-parallel scales compared to the quasi-perpendicular scales. Finally, Fig. 7f shows the resistive dissipation term; it exhibits a similar strong anisotropy to the Hall cascade rate K_{Hall}.

The compressive effects that lead to large oscillations of Ψ_c lead to important and anisotropic oscillations of $\partial_t S$, K_{MHD}, and Ψ mainly on large scales. However, further analysis of this phenomenon is beyond the scope of this paper.

5. Discussion

In this paper we studied decaying plasma turbulence using the 3D hybrid code. The spectral properties of the simulated system are similar to those in previous works (Markovskii & Vasquez 2011; Franci et al. 2018b). We concentrated our analysis of turbulence on the KHM equation (in the form that can be easily calculated using the fast Fourier transform Banerjee & Galtier 2017; Hellinger et al. 2021a; Montagud-Camps et al. 2022). The KHM results show how turbulence evolves from large-scale zero-cross helicity Alfvénic-like fluctuation. The non-linear

coupling leads to a transfer (cascade) of energy to small scales and the resistive dissipation rate slowly increases until it becomes quasi-stationary. On the other hand, the pressure–strain rate starts to be important early in the simulation and continues to be strong (i.e., of the same order as the resistive dissipation rate) during the whole simulation and exhibits important temporal variations. These oscillations are caused by the compressive part of the pressure–strain interaction that leads to largely reversible energy exchanges between the kinetic+magnetic energy and the internal energy; analogous behaviour is observed in hydrodynamic simulations (Hellinger et al. 2021b). In contrast, the incompressible (Pi-D) part of the pressure–strain coupling works as an effective dissipation mechanism. Our results suggest that the compressibility effects tend to be negligible for a good statistical sample; in our case we took a spatio-temporal average, these effects may be important locally and may affect for instance the cascade rates estimated from observations based on limited time intervals (Marino & Sorriso-Valvo 2023).

The onset of turbulence quantified using the KHM equation is similar to the results of the 2D Hall MHD simulations (Hellinger et al. 2021a), except that the pressure–strain effective dissipation appears early in the simulation. After the system reaches a quasi-stationary state it exhibits an overall behaviour similar to that of 2D hybrid simulations: the fluctuating (kinetic+magnetic) energy decreases at large scales; at intermediate scales the energy cascades via the MHD non-linear coupling. The MHD cascade partially continues to small scales through the Hall term, but the small scales are dominated by the resistive dissipation; however, the pressure–strain effective dissipation takes place over a wide range of scales. The isotropised view of the KHM equation is semi-quantitatively similar to the 2D results (Hellinger et al. 2022). The oscillations of the compressive pressure–strain rate is accompanied by variations of the decay and the MHD cascade rates that are typically more important at larger scales.

The presence of the ambient magnetic field induces a strong anisotropy similar to that observed in 3D MHD simulations (Verdini et al. 2015; Montagud-Camps et al. 2022), even though the KHM equation is only very weakly dependent on $\boldsymbol{B}_0$ (as clearly seen in its equivalent form, Eq. (3) of Hellinger et al. 2021a). The turbulent processes have similar anisotropic behaviour; they are weakly anisotropic on large scales (owing to the isotropic initialisation), and the anisotropy gets stronger towards smaller scales. The energy-containing range where the fluctuating energy decays is weakly anisotropic and importantly varies with time due to the compressive effects. The MHD cascade rate tends to be constant within an anisotropic range of scales. The Hall cascade rate is nearly stationary and strongly anisotropic; the onset of the Hall effect shifts to larger scales at quasi-parallel angles (with respect to the ambient magnetic field) compared to the quasi-perpendicular angles. The resistive dissipation is also nearly stationary and exhibits an anisotropy similar to that of the Hall cascade rate. The pressure–strain coupling is also anisotropic, works on a relatively wide range of scales, and has a weak anisotropy on large scales and strong one on small scales.

In the isotropised version of the KHM equation we have a relatively clear interpretation of the different terms. The cascade rates K_{MHD} and K_{Hall} represent the (magnetic+kinetic energy) cascade rates and $\partial_t S$, D, and Ψ have cumulative properties (cf. Hellinger et al. 2021a) as can be seen when comparing the KHM results to the results of the isotropic spectral transfer analysis (see Appendix A). The interpretation of the anisotropic terms is less clear. The behaviours of $\partial_t S$, D, and Ψ suggest some

sort of cumulative properties. We tried a few spectral transfer analyses with some anisotropic filters (cylindrical or ellipsoid) and found only a qualitative similarity to the anisotropic KHM results. The cascade rates K_{MHD} and K_{Hall} seem to have the tendency to be constant in a region that is anisotropically distributed in the $(l_\perp, l_\parallel)$. However, they are just scalars and indicate nothing about the direction of the cascading energy. The third-order structure function vectors in the usual form of the KHM equation possibly contain information about the direction of the cascade (cf. Verdini et al. 2015), but this assumption is not physically justified. Our simulation results, and previous results as well, indicate that turbulence develops in the inertial range $K(l_\perp, l_\parallel) = Q$ with (generally anisotropic) outer scales connected with the initial conditions (or injection) properties. The turbulent cascade develops an important anisotropy that induces an anisotropy at the dissipation scales, and Hall scales as well.

The KHM equation is nicely satisfied in the simulation indicating that the kinetic plasma system and different turbulent processes are clearly numerically resolved. However, the simulation box size is not well separated from the ion characteristic scales owing to the computational constraints. Moreover, the ion pressure–strain coupling sets in at relatively large scales ($\sim 10 d_i$) compared to the ion characteristic scales d_i and ρ_i. This is likely a reason for the fast onset and strong oscillations of the compressive pressure–strain rate, the decay, and the MHD cascade rate. We expect that for a larger system (and larger driving scales) the temporal variations would be reduced. This would justify our use of time-averaging to improve the statistics of turbulent fluctuations and to reduce the compressibility effects. More work is needed with a better separation between the injection (energy containing) range and the scale of the pressure–strain coupling. We presented one case study of plasma turbulence; more simulations are necessary to assess the role of the amplitude of turbulent fluctuations $\delta B/B_0$ and plasma betas, as well as the cross-helicity (Montagud-Camps et al. 2022).

References

Aluie, H. 2011, Phys. Rev. Lett., 106, 174502
Arró, G., Califano, F., & Lapenta, G. 2022, A&A, 668, A33
Banerjee, S., & Galtier, S. 2017, J. Phys. A, 50, 015501
Cassak, P. A., & Barbhuiya, M. H. 2022, Phys. Plasmas, 29, 122306
de Kármán, T., & Howarth, L. 1938, Proc. Royal Soc. London Ser. A, 164, 192
Del Sarto, D., Pegoraro, F., & Califano, F. 2016, Phys. Rev. E, 93, 053203
Eyink, G. L., & Aluie, H. 2009, Phys. Fluids, 21, 115107
Ferrand, R., Galtier, S., Sahraoui, F., et al. 2019, ApJ, 881, 50
Franci, L., Hellinger, P., Matteini, L., Verdini, A., & Landi, S. 2016, in Proc. 14th Int. Solar Wind Conf., AIP, 1720
Franci, L., Hellinger, P., Guarrasi, M., et al. 2018a, J. Phys.: Conf. Ser., 1031, 012002
Franci, L., Landi, S., Verdini, A., Matteini, L., & Hellinger, P. 2018b, ApJ, 853, 26
Franci, L., Papini, E., Micera, A., et al. 2022, ApJ, 936, 27
Galtier, S. 2008, Phys. Rev. E, 77, 015302
Ghosh, S., & Goldstein, M. L. 1997, J. Plasma Phys., 57, 129
Goldreich, P., & Sridhar, S. 1995, ApJ, 438, 763
Grete, P., O'Shea, B. W., Beckwith, K., Schmidt, W., & Christlieb, A. 2017, Phys. Plasmas, 24, 092311
Hellinger, P., Verdini, A., Landi, S., Franci, L., & Matteini, L. 2018, ApJ, 857, L19
Hellinger, P., Papini, E., Verdini, A., et al. 2021a, ApJ, 917, 101
Hellinger, P., Verdini, A., Landi, S., et al. 2021b, Phys. Rev. Fluids, 6, 044607
Hellinger, P., Montagud-Camps, V., Franci, L., et al. 2022, ApJ, 930, 48
Kida, S., & Orszag, S. A. 1990, J. Sci. Comput., 5, 85
Manzini, D., Sahraoui, F., Califano, F., & Ferrand, R. 2022, Phys. Rev. E, 106, 035202

Marino, R., & Sorriso-Valvo, L. 2023, Phys. Rep., 1006, 1
Markovskii, S. A., & Vasquez, B. J. 2011, ApJ, 739, 22
Matthaeus, W. H., Goldstein, M. L., & Roberts, D. A. 1990, J. Geophys Res., 95, 20673
Matthaeus, W. H., Yang, Y., Wan, M., et al. 2020, ApJ, 891, 101
Matthews, A. 1994, J. Comput. Phys., 112, 102
Mininni, P. D., & Pouquet, A. 2009, Phys. Rev. E, 80, 025401
Mininni, P. D., Alexakis, A., & Pouquet, A. 2007, J. Plasma Phys., 73, 377
Monin, A. S., & Yaglom, A. M. 1975, Statistical Fluid Mechanics: Mechanics of Turbulence (Cambridge: MIT Press)
Montagud-Camps, V., Hellinger, P., Verdini, A., et al. 2022, ApJ, 938, 90
Montgomery, D., & Turner, L. 1981, Phys. Fluids, 24, 825
Oughton, S., & Matthaeus, W. H. 2020, ApJ, 897, 37
Oughton, S., Matthaeus, W. H., Wan, M., & Osman, K. T. 2015, Phil. Trans. R. Soc. A, 373, 20140152
Papini, E., Franci, L., Landi, S., et al. 2019, ApJ, 870, 52
Papini, E., Hellinger, P., Verdini, A., et al. 2021, Atmosph., 12, 1632
Parashar, T. N., & Matthaeus, W. H. 2016, ApJ, 832, 57
Pezzi, O., Liang, H., Juno, J. L., et al. 2021, MNRAS, 505, 4857
Politano, H., & Pouquet, A. 1998a, Geophys. Res. Lett., 25, 273
Politano, H., & Pouquet, A. 1998b, Phys. Rev. E, 57, R21
Servidio, S., Valentini, F., Perrone, D., et al. 2015, J. Plasma Phys., 81, 325810107
Shebalin, J. V., Matthaeus, W. H., & Montgomery, D. 1983, J. Plasma Phys., 29, 525
Verdini, A., Grappin, R., Hellinger, P., Landi, S., & Müller, W. C. 2015, ApJ, 804, 119
Yang, Y., Matthaeus, W. H., Parashar, T. N., et al. 2017, Phys. Plasmas, 24, 072306
Yang, Y., Matthaeus, W. H., Roy, S., et al. 2022, ApJ, 929, 142
Yordanova, E., Vörös, Z., Sorriso-Valvo, L., Dimmock, A. P., & Kilpua, E. 2021, ApJ, 921, 65

Appendix A: Isotropic spectral transfer

Another way to analyse the scale dependence of turbulence and its processes is spectral (Fourier) decomposition (cf. Mininni et al. 2007; Grete et al. 2017). To characterise turbulence it is possible to use isotropic low-pass filtered kinetic+magnetic energy (i.e., the energy in modes with wave-vector magnitudes smaller than or equal to k; cf. Hellinger et al. 2021b)

$$E_k = \frac{1}{2} \sum_{|\boldsymbol{k}'| \leq k} \left(|\widehat{\boldsymbol{w}}|^2 + |\widehat{\boldsymbol{B}}|^2 \right), \tag{A.1}$$

where the wide hat denotes the Fourier transform. For E_k we obtained the following dynamic equation

$$\partial_t E_k + S_{\mathrm{MHD}k} + S_{\mathrm{Hall}k} = -\Psi_k - D_k, \tag{A.2}$$

where $S_{\mathrm{MHD}k}$ and $S_{\mathrm{Hall}k}$ represent the MHD and Hall energy transfer rates, respectively; Ψ_k describes the pressure–strain effect; and D_k is the resistive dissipation rate for modes with wave-vector magnitudes smaller than or equal to k. They can be expressed as

$$S_{\mathrm{MHD}k} = \Re \sum_{|\boldsymbol{k}'| \leq k} \left[\widehat{\boldsymbol{w}}^* \cdot \widehat{(\boldsymbol{u} \cdot \boldsymbol{\nabla})\boldsymbol{w}} + \frac{1}{2} \widehat{\boldsymbol{w}}^* \cdot \widehat{\boldsymbol{w}(\boldsymbol{\nabla} \cdot \boldsymbol{u})} \right.$$
$$\left. - \widehat{\boldsymbol{w}}^* \cdot \widehat{\rho^{-1/2} \boldsymbol{J} \times \boldsymbol{B}} - \widehat{\boldsymbol{B}}^* \cdot \boldsymbol{\nabla} \times \widehat{(\boldsymbol{u} \times \boldsymbol{B})} \right], \tag{A.3}$$

$$S_{\mathrm{Hall}k} = \Re \sum_{|\boldsymbol{k}'| \leq k} \widehat{\boldsymbol{B}}^* \cdot \boldsymbol{\nabla} \times \widehat{(\boldsymbol{j} \times \boldsymbol{B})}, \tag{A.4}$$

$$\Psi_k = \Re \sum_{|\boldsymbol{k}'| \leq k} \widehat{\boldsymbol{w}}^* \cdot \widehat{\rho^{-1/2} \boldsymbol{\nabla} \cdot \mathbf{P}}, \tag{A.5}$$

$$D_k = \eta \sum_{|\boldsymbol{k}'| \leq k} |\boldsymbol{k}'|^2 |\widehat{\boldsymbol{B}}|^2. \tag{A.6}$$

In these expression the asterisk denotes the complex conjugate, and $\Re$ denotes the real part. For fully developed turbulence $S_{\mathrm{MHD}k}$ and $S_{\mathrm{Hall}k}$ are the MHD and Hall cascade rates, respectively.

Similarly to the KHM case, we defined the validity test of the spectral transfer (ST) equation, Eq. (A.2), as

$$O_k = \partial_t E_k + S_{\mathrm{MHD}k} + S_{\mathrm{Hall}k} + \Psi_k + D_k. \tag{A.7}$$

Figure A.1 shows the ST validity test O_k and the contributing terms as functions of k averaged over the time interval $200 \leq t\Omega_{\mathrm{i}} \leq 300$.

Figure A.2 displays a direct comparison between the ST and KHM contributing terms as a function of k (through the inverse proportionality $kl = \sqrt{3}$. Figure A.2 shows that the MHD and Hall cascade rates in both the approaches are comparable

$$S_{\mathrm{MHD}k} \simeq K_{\mathrm{MHD}}, \quad S_{\mathrm{Hall}k} \simeq K_{\mathrm{Hall}}. \tag{A.8}$$

The MHD cascade term dominates at scales where the total power spectrum is close to a $k^{-5/3}$ power law. The other terms in the ST and KHM approaches are complementary:

$$\partial_t \left[E_k + S(l) \right] \simeq -Q, \quad D_k + D(l) \simeq Q_\eta, \quad \Psi_k + \Psi(l) \simeq \psi. \tag{A.9}$$
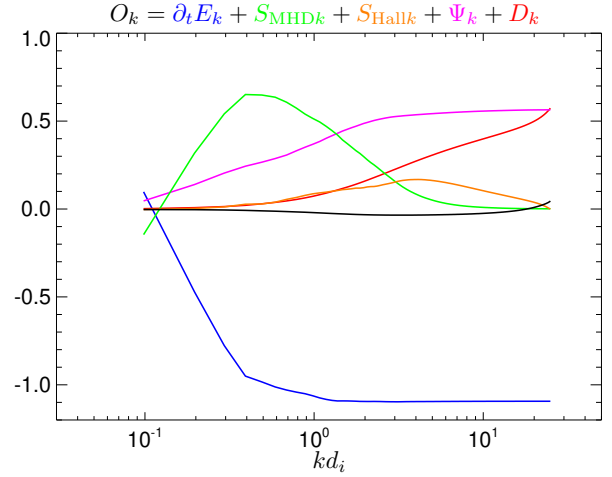

Fig. A.1. Spectral transfer analysis, the validity test of the isotropic ST O_k, Eq. (A.7), as a function of k (averaged over the time interval $200 \leq t\Omega_{\mathrm{i}} \leq 300$) (black line) along with the different contributing terms: decay rate $\partial_t E_k$ (blue), MHD cascade rate $S_{\mathrm{MHD}k}$ (green), Hall cascade rate $S_{\mathrm{Hall}k}$ (orange), resistive dissipation rate D_k (red), and pressure–strain rate Ψ_k (magenta). All the quantities are given in units of the total (effective) heating rate Q.
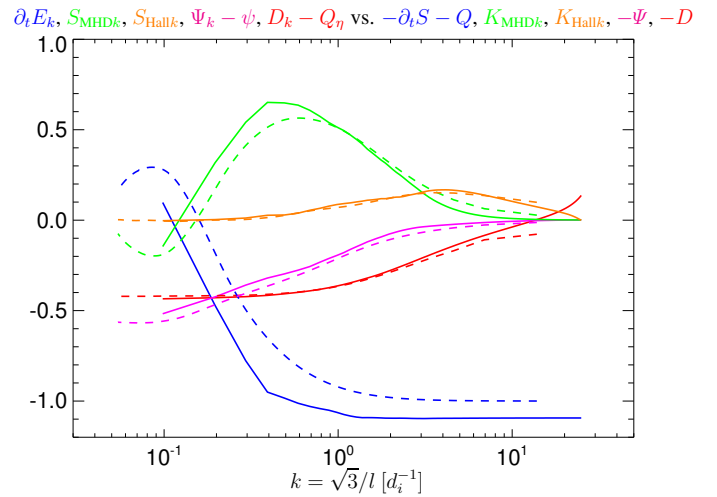

Fig. A.2. Comparison between the ST and KHM approaches. The solid lines show the contributing terms of the ST equation as a function of k: (blue) the decay rate $\partial_t E_k$, (green) the MHD cascade rate $S_{\mathrm{MHD}k}$, (orange) the Hall cascade rate $S_{\mathrm{Hall}k}$, (red) the dissipation rate $D_k - Q$, and (magenta) the pressure–strain rate $\Psi_k - \psi$. The dashed lines show the corresponding results of the KHM equation function of k through the relation $l = \sqrt{3}/k$: (blue) the decay rate $-\partial_t S - Q$, (green) the MHD cascade rate K_{MHD}, (orange) the Hall cascade rate K_{Hall}, (red) the dissipation rate $-D$, and (magenta) the pressure–strain rate $-\Psi$. All the quantities are given in units of the total (effective) dissipation rate Q.

This means that $\partial_t E_k$ represents the rate of change of the kinetic energy at scales with wave-vector magnitudes smaller than or equal to k, whereas $\partial_t S$ represents approximately the rate for wave-vector magnitudes larger than k (with $l \simeq \sqrt{3}/k$). Similarly, D_k (Ψ_k) is the dissipation (pressure–strain) rate on scales $\leq k$, whereas $D(l)$ ($\Psi(l)$) represents the corresponding rate on scales $> k$.